Available online at www.sciencedirect.com
SCIENCE DIRECT
Polymer 46 (2005) 3343–3354
polymer
www.elsevier.com/locate/polymer

# Polyamide-6,6/in situ silica hybrid nanocomposites by sol–gel technique: synthesis, characterization and properties

Rajatendu Sengupta[a], Abhijit Bandyopadhyay[a], Sunil Sabharwal[b], Tapan K. Chaki[a], Anil K. Bhowmick[a,*]

[a]*Rubber Technology Center, Indian Institute of Technology, Kharagpur 721302, India*
[b]*RTDS, Bhabha Atomic Research Center, Trombay, Mumbai 400085, India*

Received 8 October 2004; received in revised form 7 February 2005; accepted 22 February 2005

**Abstract**

The organic–inorganic hybrid nanocomposites comprising of poly(iminohexamethyleneiminoadipoyl), better known as Polyamide-6,6 (abbreviated henceforth as PA66), and silica ($SiO_2$) were synthesized through sol–gel technique at ambient temperature. The inorganic phase was generated in situ by hydrolysis–condensation of tetraethoxysilane (TEOS) in different concentrations, under acid catalysis, in presence of the organic phase, PA66, dissolved in formic acid. Infrared (IR) spectroscopy was used to monitor the microstructural evolution of the silica phase in the PA66 matrix. Wide angle X-ray scattering (WAXS) studies showed that the crystallinity in PA66 phase decreased with increasing silica content. Atomic force microscopy (AFM) of the nanocomposite films revealed the dispersion of $SiO_2$ particle with dimensions of $<100$ nm in the form of network as well as linear structure. X-ray silicon mapping further confirmed the homogeneous dispersion of the silica phase in the bulk of the organic phase. The melting peak temperatures slightly decreased compared to neat PA66, while an improvement in thermal stability by about 20 °C was achieved with hybrid nanocomposite films, as indicated by thermogravimetric analysis (TGA). Dynamic mechanical analysis (DMA) exhibited significant improvement in storage modulus ($E'$) for the hybrid nanocomposites over the control specimen. An increase in Young's modulus and tensile strength of the hybrid films was also observed with an increase in silica content, indicating significant reinforcement of the matrix in the presence of nanoparticles. Some properties of the in situ prepared PA66-silica nanocomposites were compared with those of conventional composites prepared using precipitated silica as the filler by solution casting from formic acid.


*Keywords:* Sol–gel; Polyamide-6,6; Nanocomposites

## 1. Introduction

Inorganic–organic hybrid nanocomposites using the sol–gel process where the inorganic phase is grown in situ is being actively pursued globally [1–3]. The shift in emphasis from the traditional practice of mechanically blending the reinforcing fillers into a polymeric matrix to the sol–gel process is due mostly to the subtle control over morphology and/or surface characteristics of the growing inorganic phase in the polymer matrix by control of various reaction parameters like pH, concentration, temperature, etc. More importantly, unlike the traditional composites, which have macroscale domain size varying from micrometer to millimeter scale, the inorganic–organic hybrids have domain sizes varying typically from 1 to 100 nm [4]. Thus, the inorganic–organic hybrids are usually optically transparent, even though microphase separation may exist. Sol–gel hybrid preparation mostly centers on the growth of the inorganic phase from the hydrolysis–condensation of alkoxysilanes like TEOS in a solution containing the organic polymer. The mechanism of hydrolysis–condensation of TEOS is well known [5]. Scheme 1 depicts the formation of the three-dimensional silica network arising as an outcome of the hydrolysis and condensation reactions of TEOS. So far, many hybrids have been prepared in this way using poly(vinyl acetate) [6,7], poly(methyl methacrylate) [8,9], poly(vinyl pyrrolidone) [9], poly(ethylene oxide)

* Corresponding author. Tel.: +91 3222 283180/220312; fax: +91 3222 277190/220312.
*E-mail address:* anilkb@rtc.iitkgp.ernet.in (A.K. Bhowmick).

0032-3861/$ - see front matter © 2005 Elsevier Ltd. All rights reserved.
doi:10.1016/j.polymer.2005.02.104

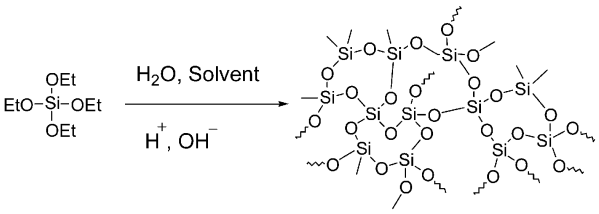


Scheme 1. Overall scheme for the formation of 3D silica network by hydrolysis and condensation of TEOS.

[10], poly(dimethylsiloxane) [11], Nafion® [12,13], poly (vinyl alcohol) [14] and several other polymers. From our laboratory, we have reported several nanocomposites including those prepared by the sol–gel technique [15–18].

The novelty of this work lies in the fact that the silica nanophase has been grown in situ within the Polyamide-6,6 (PA66) matrix probably for the first time. The present paper describes a comparison of spectroscopic, morphological, thermal, mechanical, dynamic mechanical and water absorption properties of silica composites with those of PA66 and an attempt has been made to explain the properties with the structure of the nanocomposites. For comparison, optical and morphological properties of precipitated silica-PA66 composites prepared by solution blending technique have been reported. It is worth mentioning that nanocomposites based on polyamides (particularly polyamide-6) and nanoclay has commercial potential [19].

## 2. Experimental

### 2.1. Preparation of PA66-silica nanocomposites

A commercial grade of PA66 (Zytel 101L, DuPont, India) was dissolved in 85% formic acid (synthesis grade, Merck Ltd., India) to prepare a 10 wt% PA66 solution. Different amounts of TEOS (Acros Organics, USA, density = 0.93) were carefully added to this 10 wt% PA66 solution with vigorous stirring with a magnetic stirrer bar at room temperature (30 °C). No water was added externally, as water was already present in the formic acid to the extent of 12–15%. The stirring was carried out for 1 h under ambient conditions of ~30 °C and ~80% relative humidity to get the feed proportions of 1, 2, 3, 4, 5, 10 and 15 wt% of TEOS based on the amount of PA66. The solutions in beakers were covered with polyethylene (PE) films and allowed to stand at room temperature for 12 h to allow the hydrolysis and condensation reactions of TEOS to continue and were then finally poured onto thoroughly cleaned glass plates for room temperature drying in a fume hood to constant weight. The air-dried films on the glass plates were opaque and extremely adherent and thus had to be scrapped with a stainless steel spatula for removal. The resultant films were vacuum dried for 24 h at 80 °C and subsequently compression molded in between Teflon sheets at 280 °C for 6 min for obtaining self-standing films having thickness ~100–150 μm ready for testing. The films were stored in a desiccator to minimize moisture ingress. However, during synthesis and testing of the hybrid composite films, the relative humidity in air was ~80%. All the films were prepared at the same time and thus were subjected equally to the ambient conditions of temperature and humidity.

Pure PA66 films were prepared in the same manner, which also showed opaqueness and milk-white color upon drying of the solvent but became transparent after compression molding. Conventional composite films were also prepared in the same manner by using precipitated silica (Ultrasil VN 3, Bayer Ltd., India, particle size range = 20–100 nm, pH = 6). However, the loading of precipitated silica was kept at 3 and 5 wt% based on the amount of PA66 solely for comparative purposes. Composition of the hybrid composites along with the appearance of the films is reported in detail in Table 1. In all the cases, the results are compared with neat PA66 film prepared under similar conditions.

### 2.2. Characterization of PA66-silica nanocomposites

The silica content in the nanocomposites was determined experimentally by gravimetric analysis using a muffle furnace (samples were held at 800 °C for 9 h in air and the residue remaining was taken to be the silica content of the sample). The results of different compositions are tabulated in Table 1. For the in situ prepared nanocomposites, the theoretical silica wt% was calculated by assuming complete condensation of TEOS. In the Section 3, the samples are referred by the sample designations listed in Table 1 which are based on the TEOS wt% used in the feed charge.

IR spectroscopic analyses were carried out under ambient conditions using a Perkin–Elmer 843 spectrophotometer in the spectral range from 4000 to 200 $cm^{-1}$ at a resolution of 2.4 $cm^{-1}$. Transmittance measurement of the films was performed in the visible wavelength range of 400–700 nm using a GENESYS™ 2 UV/visible spectrophotometer (ThermoSpectronic, USA).

Tapping mode AFM images were obtained with a Veeco-Digital Instruments Multimode SPM (scanning probe microscopy) with Nanoscope IIIa with tapping mode (model RTESP) probes for morphological investigation. The specified resonance frequency of these tips was ~280 kHz. Small squares ($2 \times 2$ $mm^2$) of PA66/silica nanocomposites were cut from the nanocomposite films and attached to stainless steel sample puck for AFM imaging. Typical scan rate for image acquisition was ~1.004 lines/s. All images were obtained under ambient laboratory conditions. No filtering or other image processing operations were performed to generate the images.

The films were sputter-coated with gold to take the SEM images of the film surfaces at an accelerating voltage of 10 kV. The distribution of Si atoms in the hybrid composites

Table 1
Composition of the prepared samples

| Sample Code | PA66 (%) | TEOS (%) | Ultrasil VN3 (%) | Silica (wt%) | | Appearance of the films |
|---|---|---|---|---|---|---|
| | | | | Theoretical[a] | Experimental[b] | |
| N66T0 | 100 | 0 | – | 0.0 | 0.0 | Transparent |
| N66T1 | 100 | 1 | – | 0.3 | 0.2 | Transparent |
| N66T2 | 100 | 2 | – | 0.6 | 0.5 | Transparent |
| N66T3 | 100 | 3 | – | 0.9 | 0.8 | Transparent |
| N66T4 | 100 | 4 | – | 1.2 | 1.1 | Transparent |
| N66T5 | 100 | 5 | – | 1.5 | 1.4 | Transparent |
| N66T10 | 100 | 10 | – | 3.0 | 2.7 | Slight hazy |
| N66T15 | 100 | 15 | – | 4.5 | 4.3 | Hazy |
| N66V3 | 100 | – | 3 | 3.0 | 2.9 | Hazy |
| N66V5 | 100 | – | 5 | 5.0 | 4.8 | Hazy |

[a] The weight percent $SiO_2$ was calculated assuming full condensation of TEOS.
[b] Residue from gravimetric analysis carried out in a muffle furnace in air at 800 °C.

was recorded in an Oxford ISIS 300 EDX system attached to the JEOL JSM 5800 scanning electron microscope. The white points in the figures denote Si signals.

Wide angle X-ray scattering (WAXS) data were collected in digital form from the films using a Philips 1710 X-ray diffractometer operated at 40 kV and 20 mA with Cu $K_\alpha$ radiation source. The scan rate was 3°/min. The crystallinity was calculated following the method outlined in our previous publication [20].

Differential scanning calorimetry (DSC) measurements of the pure PA66 and the PA66-silica nanocomposites were performed using a DSC model Q 100 of TA Instruments-Waters LLC, USA in the temperature range from 30 to 300 °C at a heating (or cooling) rate of 10 °C/min under nitrogen atmosphere. For determining the crystallinity from the DSC heating run, the heat of fusion of a 100% crystalline PA66 was taken to be 190 J/g [21]. Thermal stability of the films was analyzed using TGA Q 50 of TA Instruments-Waters LLC, USA at a heating rate of 10 °C/min in the temperature range of 40–800 °C under nitrogen atmosphere.

The measurements of mechanical properties of the composites were carried out using a Zwick 1445 universal testing machine at a crosshead speed of 50 mm/min. The tensile specimens were punched from the compression molded films using ASTM type IV die. The tests were carried out as per ASTM D 638-98 at $25 \pm 2$ °C. The Young's modulus was calculated from the stress–strain curve below 5% strain. The average value of five tests was used for reporting.

DMA 2980 dynamic mechanical analyzer of TA Instruments-Waters LLC, USA was used in tension film mode in the temperature range of −50 to 200 °C at a frequency of 1 Hz and heating rate of 2 °C/min. The storage modulus ($E'$) and loss tangent ($\tan \delta$) were measured as a function of temperature for all the specimens under identical conditions.

Water absorption tendency of PA66 and the hybrid nanocomposites was evaluated by immersing equal weights of the sample films in water for ~120 h at ambient temperature. The water uptake was calculated using the following formula:

$$\%\text{Water uptake} = \frac{(\text{Final weight} - \text{Initial weight})}{\text{Initial weight}} \times 100 \quad (1)$$

## 3. Results and discussion

### 3.1. IR studies

The IR spectrum of N66T0 (neat PA66) and N66T5 are shown in Fig. 1(a) with all the characteristic peaks labeled. Neat PA66 films show the characteristic peaks at 3320 $cm^{-1}$ (N–H stretch), 2938 $cm^{-1}$ ($CH_2$ stretch), 1640 $cm^{-1}$ (C=O stretch, amide I), 1540 $cm^{-1}$ (in-plane N–H deformation, amide II), 1370 $cm^{-1}$ (CN stretch + in-plane NH deformation, amide III), 1200 $cm^{-1}$ (amide III coupled with hydrocarbon skeleton) and 934 $cm^{-1}$ (C–CO stretch, crystalline band) respectively as reported previously by other researchers [22–24]. The bands at ~1020 –1080 $cm^{-1}$ in the IR spectrum of the silicate nanocomposites are assigned to the asymmetric Si–O–Si stretching and provide a measure of the degree of network polymerization [12]. (The differences between the FTIR spectra of N66T0 and N66T5 are qualitative and the quantitative aspect becomes clear when Fig. 1(b) is considered as discussed below.) The ~800 $cm^{-1}$ vibration is associated with symmetric Si–O–Si skeletal stretching, while the 460 $cm^{-1}$ band appears due to Si–O–Si bending mode. The bands observed in the region ~930–950 $cm^{-1}$ are assigned to Si–OH (silanol) stretching and broad bands centered near 3400 $cm^{-1}$ are assigned to various hydrogen-bonded SiO–H (silanol) stretching vibrations.

Quantitative IR analysis was carried out by calculating specific absorbance ratios relevant to the presence of the

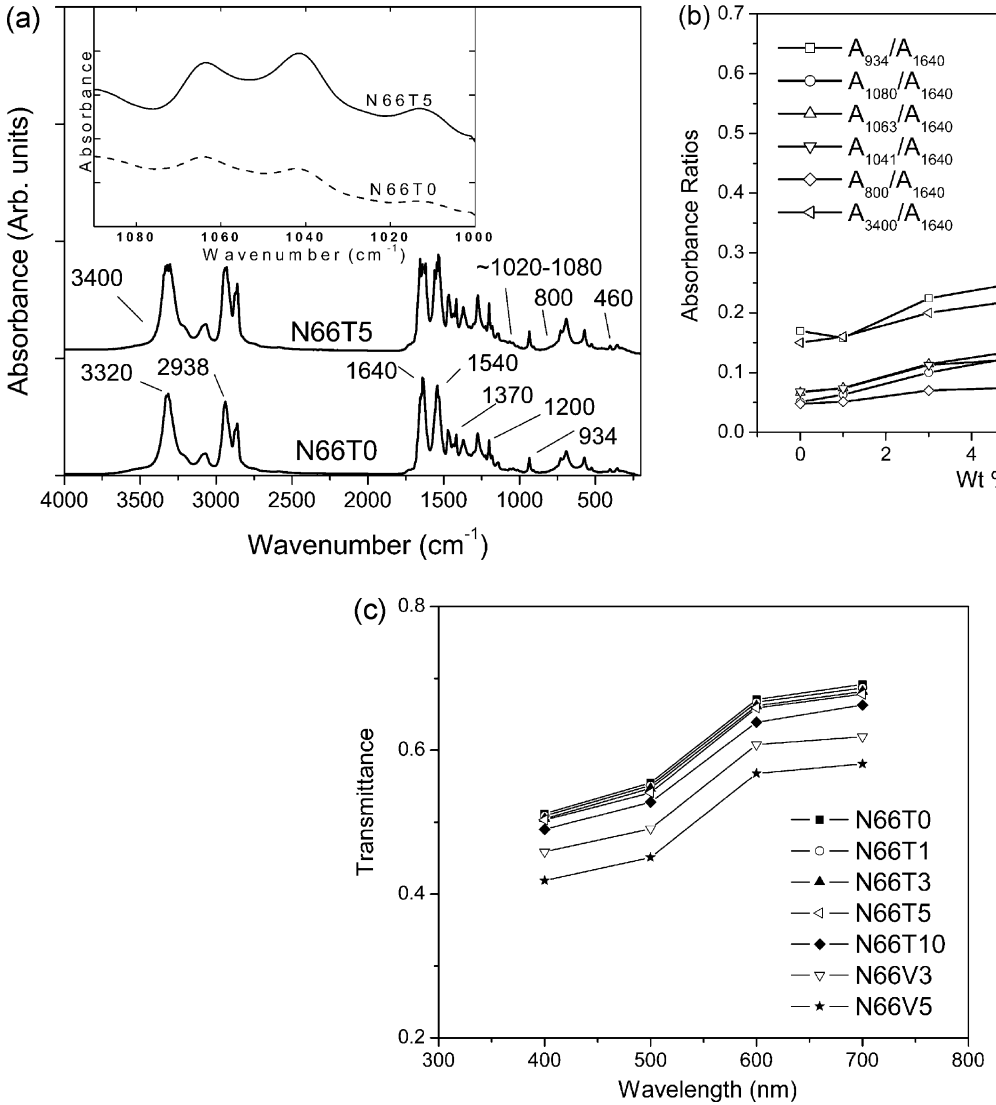


Fig. 1. (a) IR spectra of N66T0 (neat PA66) and N66T5 films having the same absorbance scale but vertically displaced for clarity. In the inset, a zoom up of the 1090–1000 $cm^{-1}$ wavenumber region shown with the original absorbance scale. (b) IR absorbance ratios versus TEOS loading for the prepared films. (c) Transmittance spectra of the compression molded film samples.

silica phase in the PA66 matrix. The absorbance value of the 1640 $cm^{-1}$ peak was taken as the internal reference band as reported by previous researchers [22,23] and was used as the denominator in the absorbance ratio calculations to eliminate the thickness variation in the compression molded films. The plots of absorbance ratio against TEOS loading for a few representative peaks are shown in Fig. 1(b). The ratio of the absorbance value at 934 $cm^{-1}$ to the absorbance value at 1640 $cm^{-1}$, represented symbolically as $A_{934}/A_{1640}$, continually increases at high TEOS loading. The band at ~934 $cm^{-1}$ for neat PA66 signifies a crystalline band as mentioned above and in the system under study the Si–OH stretching peak also occurs at the same position. The increase in the unreacted silanol groups at high TEOS loading increases the absorbance values. Since, the asymmetric Si–O–Si stretch does not show distinct peak splitting, discrimination between cyclic and linear inorganic network structures is not attempted here. The absorbance ratios $A_{1080}/A_{1640}$, $A_{1063}/A_{1640}$ and $A_{1041}/A_{1640}$ also show a general increasing trend with increasing TEOS loading. This hints at simultaneous increase in both network as well as linear structures with TEOS loading up to 3 wt%. However, from 5 wt% TEOS loading and above, the network structure formation gets predominance over linear structures. This is evident from the increasing difference in the absorbance ratio between $A_{1080}/A_{1640}$ and $A_{1041}/A_{1640}$ and between $A_{1063}/A_{1640}$ and $A_{1041}/A_{1640}$ in Fig. 1 (b). The symmetric Si–O–Si stretching vibration occurring at 800 $cm^{-1}$ also increases with increasing $SiO_2$ content as evident from the $A_{800}/A_{1640}$ ratio. The ratio $A_{3400}/A_{1640}$ also increases with increasing TEOS loading indicating the increase in silanol moieties as a result of acid catalyzed hydrolysis of TEOS in the hybrids. The increase in all the absorbance ratios indicates increased interaction between the in situ generated silica phase and PA66 and this interaction is probably in the form of labile hydrogen bonds. Thus the PA66/silica hybrid nanocomposites fall under the classification of class I materials (where the inorganic and organic components interact only weakly through hydrogen bonding, van der Waals contacts or electrostatic forces) as proposed by Sanchez and Ribot [25]. These hydrogen bonds probably reinforce the polymer structure and results in loss of flexibility of the hybrid composite films with increasing TEOS loadings (noticeable at 10% TEOS loading and above as described later).

### 3.2. Light transmittance studies

Quantitative visible light transmittances of the films are shown in Fig. 1(c). The transmittance values of the nanosized silica/PA66 hybrid composites are near to that for the neat PA66 film (N66T0) which proves that the in situ generated silica is well-dispersed within the organic matrix and their domain sizes are lower than that of visible light. However, the Vulkasil loaded PA66 composite (N66V3) is slightly more translucent compared to PA66T10, which is probably due to the aggregation and/or agglomeration of the precipitated silica particles compared to the in situ generated nanosized silica. The corresponding qualitative transparency results are tabulated in Table 1.

### 3.3. X-ray studies

WAXS was used to investigate the changes in crystalline structure of the PA66-silica nanocomposite samples. The WAXS scans of the nanocomposite samples are stacked in Fig. 2. Usually, the peaks at $2\theta$ values of ~20.2 and 23.6° signify the existence of the α phase in PA66. It was previously known that PA66 can exist only in the α and β crystalline forms at room temperature [26]. Under certain circumstances the γ crystalline phase also exists along with the α phase in PA66 at room temperature [27]. However, the α phase is more stable than the γ phase at room temperature and that is why the α→γ phase transformation in PA66 occurs much above room temperature (the well known phenomenon of Brill transition) [28].

In the present system, the α phase peaks, viz. α1 and α2 occur at ~20.2 and ~23.6°, respectively, and the γ1 peak occurs at ~13.3°. There is no γ2 peak. However, Liu et al. [27] observed both γ1 and γ2 peaks in PA66/clay nanocomposites. The α1 peak arises from the distance between the hydrogen-bonded chains and the α2 peak arises from the separation of the hydrogen-bonded sheets [29]. The peak maximum along with the corresponding *d*-spacing for the samples are tabulated in Table 2. The data in Table 2 prove that there is neither any peak shift nor any significant shift in *d*-spacing even with increase in TEOS loading from 0 to 10 wt%. This probably means that the polymerized silica occupies the free volume of the polymer. Jain et al. [30] made the observation that the non-occurrence of diffraction peaks at $2\theta$ values of ~12 and 19° in PA66 confirmed the absence of the β form of PA66. Therefore, the $2\theta$ values ranging from 13.2 to 13.4° in the present system most probably belong to the γ form of PA66. Since, the γ1 peak is present in all the samples, it confirms that it is an

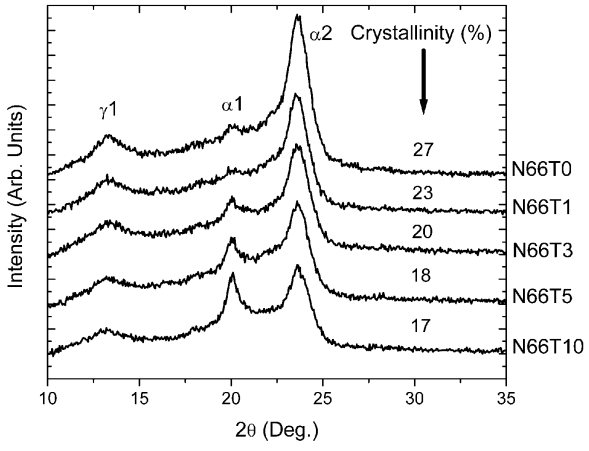


Fig. 2. WAXS scans of the unannealed films as a function of TEOS loading.

Table 2
Variation of $2\theta$ and $d$-spacing for the $\alpha1$, $\alpha2$ and $\gamma1$ peaks of the nanocomposite films

| Sample code | Parameters | Peaks | | |
|---|---|---|---|---|
| | | $\alpha1$ | $\alpha2$ | $\gamma1$ |
| N66T0 | $2\theta$ (°) | 20.2 | 23.6 | 13.4 |
| | $d$-spacing (nm) | 0.44 | 0.38 | 0.66 |
| N66T1 | $2\theta$ (°) | 20.0 | 23.5 | 13.3 |
| | $d$-spacing (nm) | 0.44 | 0.38 | 0.66 |
| N66T3 | $2\theta$ (°) | 20.1 | 23.6 | 13.4 |
| | $d$-spacing (nm) | 0.44 | 0.38 | 0.66 |
| N66T5 | $2\theta$ (°) | 20.0 | 23.6 | 13.2 |
| | $d$-spacing (nm) | 0.44 | 0.38 | 0.67 |
| N66T10 | $2\theta$ (°) | 20.1 | 23.6 | 13.2 |
| | $d$-spacing (nm) | 0.44 | 0.38 | 0.66 |

artifact of the solution casting and/or the thermal history and not due to the silica generated in situ in the system.

The near absence of the $\alpha1$ peak in N66T0 is explainable on the basis of reduced perfection of the crystallites and/or size due to the film preparation technique. Similar WAXD patterns have been observed by Haruvy et al. [31] in the nylon-6 system prepared by compression molding. They have also reported that the perfection of the crystallites and/or their size increased (as evidenced from the sharper $\alpha1$ and $\alpha2$ peaks) as a result of annealing. We obtained a similar trend in our system upon annealing of the films at 200 °C for 3 h in vacuum. However, the annealing results are not reported here. As all the films were prepared and subjected to the same conditioning, the comparison of the unannealed films is meaningful. On subsequent addition of TEOS, the $\alpha2$ peak decreases in intensity and $\alpha1$ peak intensity slowly increases as evident from Fig. 2. The decrease in the $\alpha2$ peak intensity implies loss of hydrogen bonding between C=O and N–H groups and this may be due to the interference of the silanol groups which increases quantitatively with increase in TEOS loading from 0 to 10 wt% as mentioned in the IR discussion. The percent crystallinity from WAXS is mentioned in Fig. 2 against the sample curves. This decreases with increase in TEOS loading. On addition of 1% TEOS, the drop in crystallinity is ~15% from the neat polymer. The maximum drop in crystallinity occurs for N66T10 where the crystallinity is 37% less than that in N66T0. The decrease in crystallinity is probably due to the loss in hydrogen bonding between the C=O and N–H groups situated on neighboring chains due to in situ generation of nanosized silica as mentioned above.

### 3.4. Microscopic studies

The AFM phase image for N66T5 is shown in Fig. 3(a). The presence of linear silica structures is seen to be predominant with some amount of network formation also. The lengths of the linear structures runs into the micron range while the width varies between 50 and 70 nm. Discrete nanosized silica particles (<50 nm) are also dispersed throughout the matrix. Fig. 3(b) shows the SEM micrograph of N66T5 and the presence of linear silica structures is evident.

Fig. 4 compares the Si mapping of N66T3, N66T5, N66T10 and N66V5. It is evident that there is slight aggregation of silica in the N66T10 film and substantial aggregation of silica in the N66V5 film. However, there is no aggregation in the nanocomposite films having TEOS loading of 3 and 5 wt%. Since, the agglomeration of the silica particles in N66T10 film is not very substantial, the transparency of the film is not much affected.

### 3.5. Thermal characterization of the PA66-silica nanocomposites

The PA66 melting was studied by performing DSC on N66T0, N66T3, N66T5 and N66T10. The second heating DSC traces of the samples are compared in Fig. 5. A summary of the DSC data corresponding to the curves for the heating scan are tabulated in Table 3. The data indicate that with increasing TEOS loading the melting peaks gradually decreased in comparison to neat PA66 (the heat of fusion values reflect this trend). More surprising was the fact that the in situ generated nanosized silica did not cause any increase in crystallinity. Incorporation of silica particles within the chain interstices decreases the overall crystallinity probably by reducing the hydrogen bonding interaction between C=O and N–H groups on the PA66 backbone and for this the silanol groups may be primarily responsible. From Fig. 5 it is seen that two melting peaks occur for the neat PA66 and PA66/silica nanocomposites. The higher temperature melting peak has been designated as $T_{m1}$, while the lower temperature one as $T_{m2}$ in Table 3. According to Khanna [32], this double melting phenomenon ascribed due to a bimodal crystallite distribution is common to nylons like PA66 and is a characteristic of melts crystallized at a cooling rate of 10 °C/min. Further, the appearance of the dual melting peaks in both the neat PA66 and PA66/silica nanocomposites proves that this is not due to the presence of nanosized silica generated in the system under study.

The DSC cooling scan for the unannealed films are shown in Fig. 6 and all the scans show only one exothermic peak. The peak ($T_p$) and onset of crystallization ($T_o$) temperatures are listed in Table 3 along with the respective heat of crystallization ($\Delta H_c$) values. It is seen that the presence of nanosized silica decreases the crystallization temperature. There is a decrease in the $\Delta H_c$ values with increase in TEOS loading. Similar results have been reported previously on polyamide 6-based clay nanocomposites [33].

The TGA measurements of neat PA66 and PA66/silica nanocomposites with different TEOS loadings are shown in Fig. 7. The onset of thermal degradation ($T_d$) mentioned in Fig. 7 proves that the thermal stability of the nanocomposites increases up to 3 wt% TEOS loading and then decreases thereafter with increasing TEOS loading.

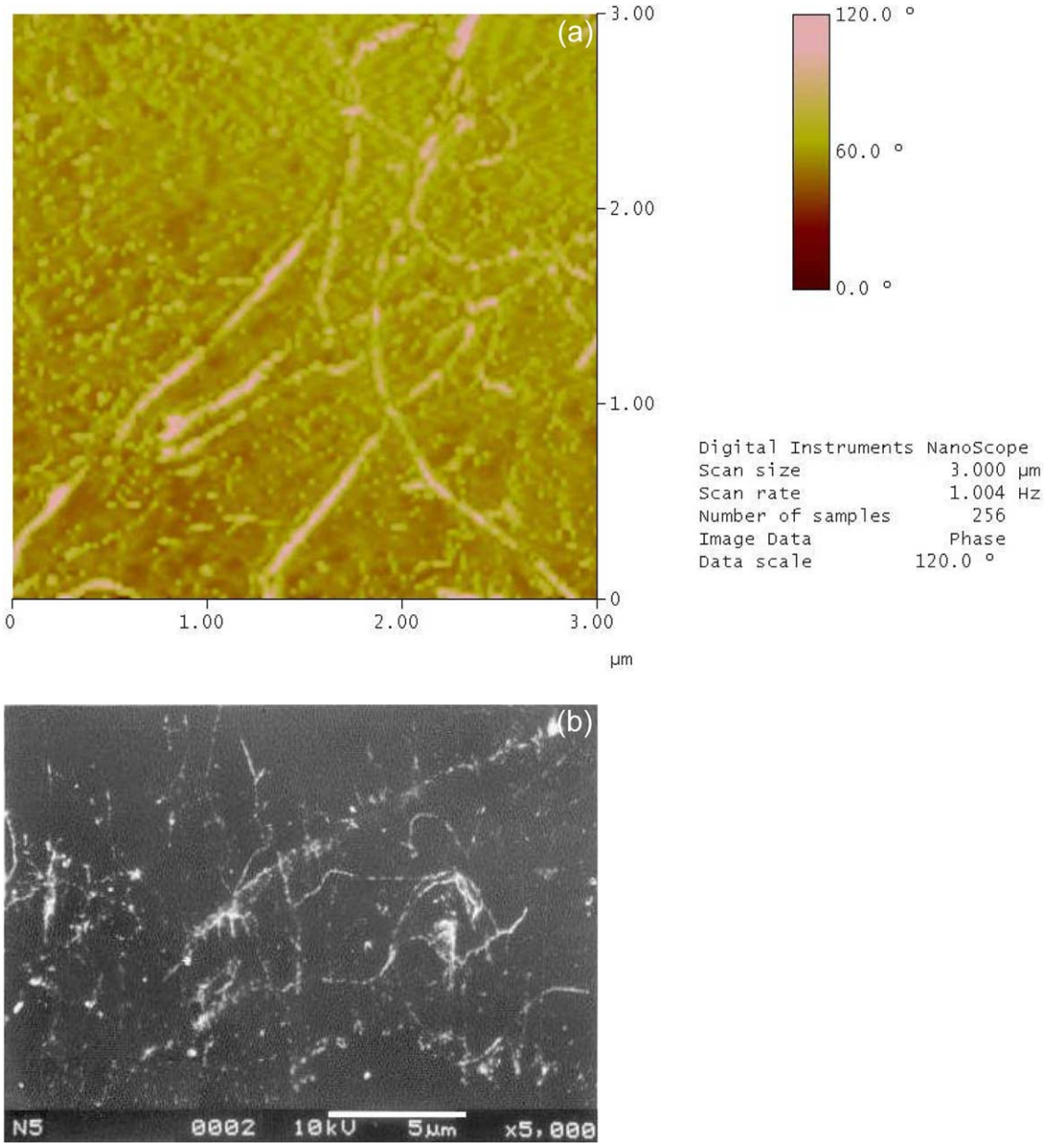


Fig. 3. (a) AFM phase image of N66T5. (b) SEM of N66T5.

However, all the TEOS loaded films showed increased $T_d$ compared to neat PA66 film. $T_d$ is shifted by 18 °C for the composite with only 0.8 wt% of silica nanoparticles. This initial increase in the thermal stability of the nanocomposites is most likely the consequence of the attachment of the PA66 chains to the surface of the in situ generated silica. This physical crosslinking network along with the residual crystallinity and other bonding forces at temperatures higher than the $T_m$ of PA66 is responsible for this thermal behavior. However, after a threshold concentration (0.8 wt% silica) is exceeded, the in situ generated silica most probably does not have much effect on the decomposition characteristics of the composites. This may be reasoned on the basis of an inherently weaker structure as a result of loss in crystallinity with increasing silica content as found out from the DSC studies. The residue left at 800 °C is in line with the experimental silica content as reported in Table 1 and this result indicates that the thermal decomposition routes of neat PA66 and PA66/silica nanocomposites are same. If the decomposition routes were different, then the residual weights of the nanocomposites would have been different. It should be noted that polyamide-6/organoclay nanocomposites showed lower thermal stability than neat polyamide-6 as reported by Cho and Paul [34]. Therefore, with as low as 0.2 wt% silica loading (corresponding to TEOS loading of 1 wt%) the thermal stability improvement of the PA66/silica nanocomposites is substantial.

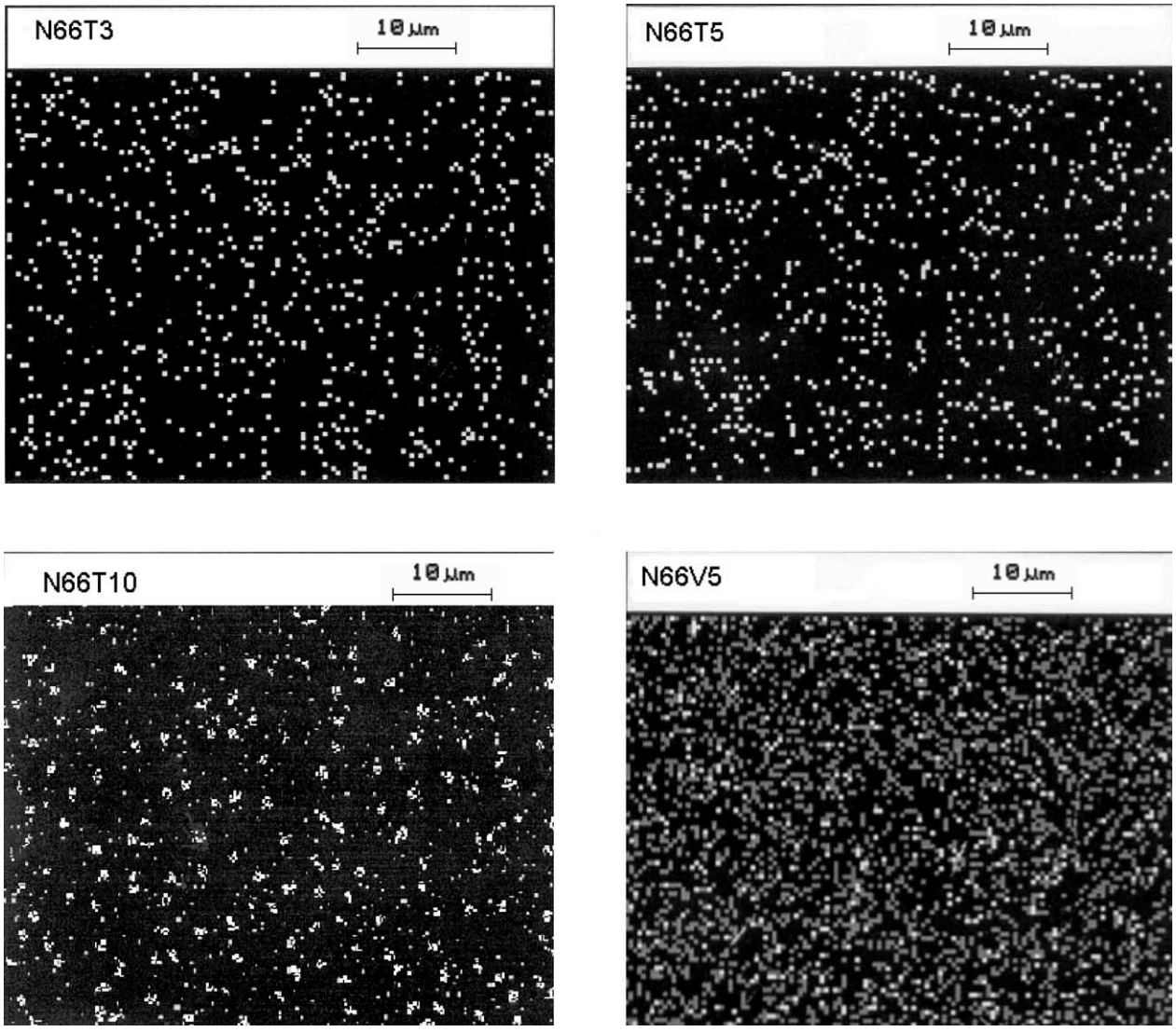


Fig. 4. Si mapping of the unannealed N66T3, N66T5, N66T10 and N66V5 films.

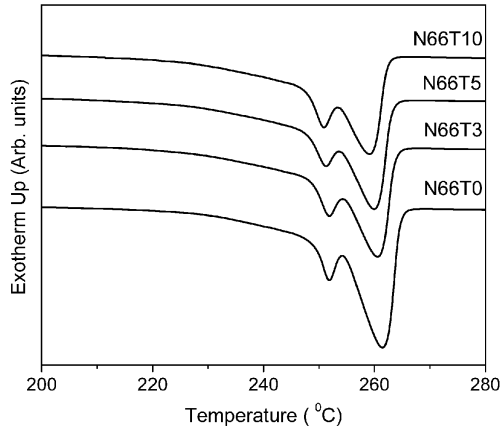


Fig. 5. DSC of unannealed films (10 °C/min, second heating). For clarity the temperature range is shown from 200 to 280 °C and the curves have been vertically displaced.

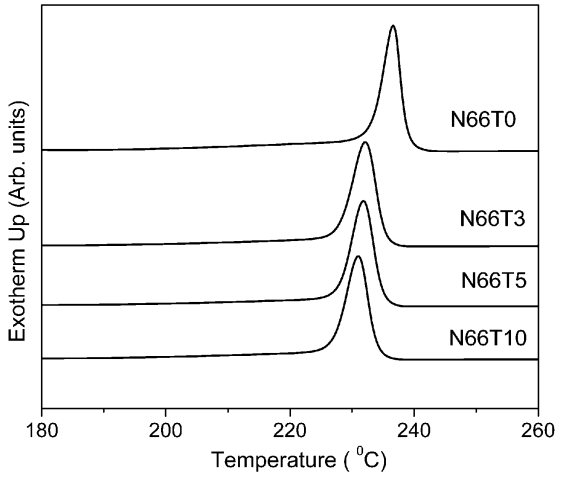


Fig. 6. DSC of unannealed films (10 °C/min, cooling scan). For clarity the temperature range is shown from 180 to 260 °C and the curves have been vertically displaced.

Table 3
Melting temperatures ($T_{m1}$, $T_{m2}$), Heat of fusion ($\Delta H_{EXP}$) and percent crystallinity from the second DSC heating scans and Heat of crystallization ($\Delta H_c$), crystallization peak ($T_p$) and onset of crystallization ($T_o$) temperatures from DSC cooling scans of the unannealed films

| Sample code | $T_{m1}$ (°C) | $T_{m2}$ (°C) | $\Delta H_{EXP}$ (J/g) | Crystallinity[a] (%) | $\Delta H_c$ (J/g) | $T_p$ (°C) | $T_o$ (°C) |
|---|---|---|---|---|---|---|---|
| N66T0 | 262 | 252 | 70 | 37 | 61 | 236 | 239 |
| N66T3 | 261 | 252 | 65 | 35 | 58 | 232 | 235 |
| N66T5 | 260 | 251 | 62 | 33 | 56 | 232 | 235 |
| N66T10 | 259 | 250 | 60 | 32 | 55 | 231 | 234 |

[a] Necessary correction was done in the $\Delta H_{EXP}$ value to get the fusion value for the neat polymer by linear weighted averaging of the PA66 and $SiO_2$ weight contributions at each composition. The weight percent $SiO_2$ in the composition was calculated assuming full condensation of TEOS.

### 3.6. Mechanical and dynamic mechanical properties of the PA66-silica nanocomposites

Typical tensile stress–strain curves for the unannealed films are presented in Fig. 8(a). Tensile stress–strain characteristics of the N66T15 film could not be determined as the film was very brittle in nature and could not be die-punched to get the tensile specimen. All the PA66/silica nanocomposite films having TEOS loading 1–10 wt% showed an increase in the Young's modulus ($E$) over neat PA66. However, the modulus value reached a maximum for the N66T5 film and then dropped to a lower value for the N66T10 film. It is well known that in semicrystalline polymers like PA66, the crystallinity plays a major role in shaping the mechanical properties. With increase in the TEOS content, the crystallinity decreased (as observed from the WAXS and DSC studies). Since, the modulus depends substantially on crystallinity for PA66, the modulus should have decreased, but instead it increased. An increase in modulus can be explained by the reinforcing action provided by the nanosized in situ generated silica particles. With only 1.5 wt% of theoretical silica content (N66T5) the modulus increased ~75% compared to neat PA66 (N66T0). The trends in the modulus, maximum tensile stress (MTS), work to break (WB) and elongation at break (EB) behavior of neat PA66 and PA66/silica nanocomposite films are compared in Fig. 8(b) and (c). The trend in each case is in line with that of the modulus and thus can be explained probably by the opposing factors of decrease in crystallinity and reinforcing action of nanosized in situ generated silica filler acting in tandem. Further, the agglomeration tendency of the in situ generated silica particles also has a role in influencing the mechanical properties of the films having TEOS loading of 10 wt% and above. It is observed that the optimization in mechanical strength is reached in the case of N66T5 and the increase in MTS, WB and EB is ~14, 425 and 193%, respectively. A similar trend was reported in the case of PEBAX®/silica nanocomposites previously [35]. The increase in EB of the PA66/silica nanocomposites over neat PA66 can be explained probably on the basis of the linear and network growths of the inorganic phase as observed from the IR and AFM studies. However, there is optimization at a TEOS loading of 5 wt%, and above that the EB gets lowered probably due to the fact that too much of silica network structures would mean agglomeration of the silica particles. Si mapping (Fig. 4) shows that aggregation/agglomeration starts from N66T10 and thereby supports this proposition. This agglomeration leads to the increasing brittle nature of the films from TEOS loading of 10 wt% and above.

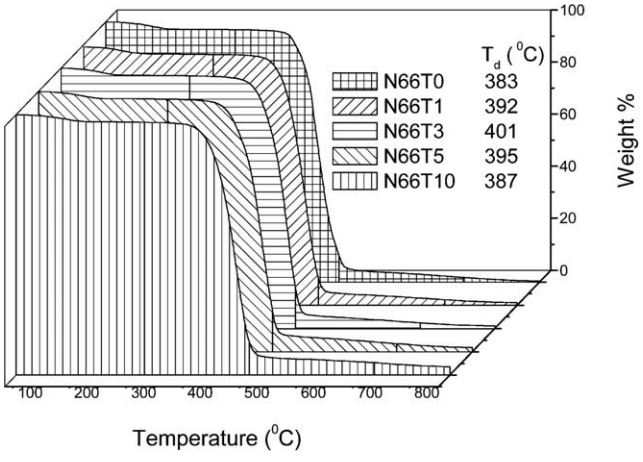


Fig. 7. TGA curves for neat PA66 and PA66/silica nanocomposites.

The variation of tan $\delta$ and storage modulus ($E'$) with temperature for the films are shown in Fig. 9(a) and (b), respectively. The $T_g$ (glass transition temperature) for N66T0 occurs at ~24 °C and for N66T5 there is a significant shift of ~+12 °C in $T_g$ from the N66T0 peak. The tan $\delta$ peak heights of all the PA66/silica nanocomposites are greater than that for the neat PA66 film, which confirms the decrease in crystallinity with increasing TEOS loading. The $T_g$ values of neat PA66 and PA66/silica nanocomposites are all below the usually reported $T_g$ value of ~70–80 °C for dry-as-molded (DAM) specimens. Since, DAM conditions were not maintained, the $T_g$ values are typically less. Further, one needs to consider that unreacted silanol groups are hydrophilic and would attract moisture from the ambient atmosphere and the existence of increasing silanol groups as mentioned in the IR discussion would increase the moisture absorbing tendency further. This gets reflected in the tan $\delta$ curves in Fig. 9(a) by almost no shift in the $T_g$ values (in the case of N66T1 and N66T3) even though there is a significant improvement in the storage modulus values with increased TEOS loading as noticed from

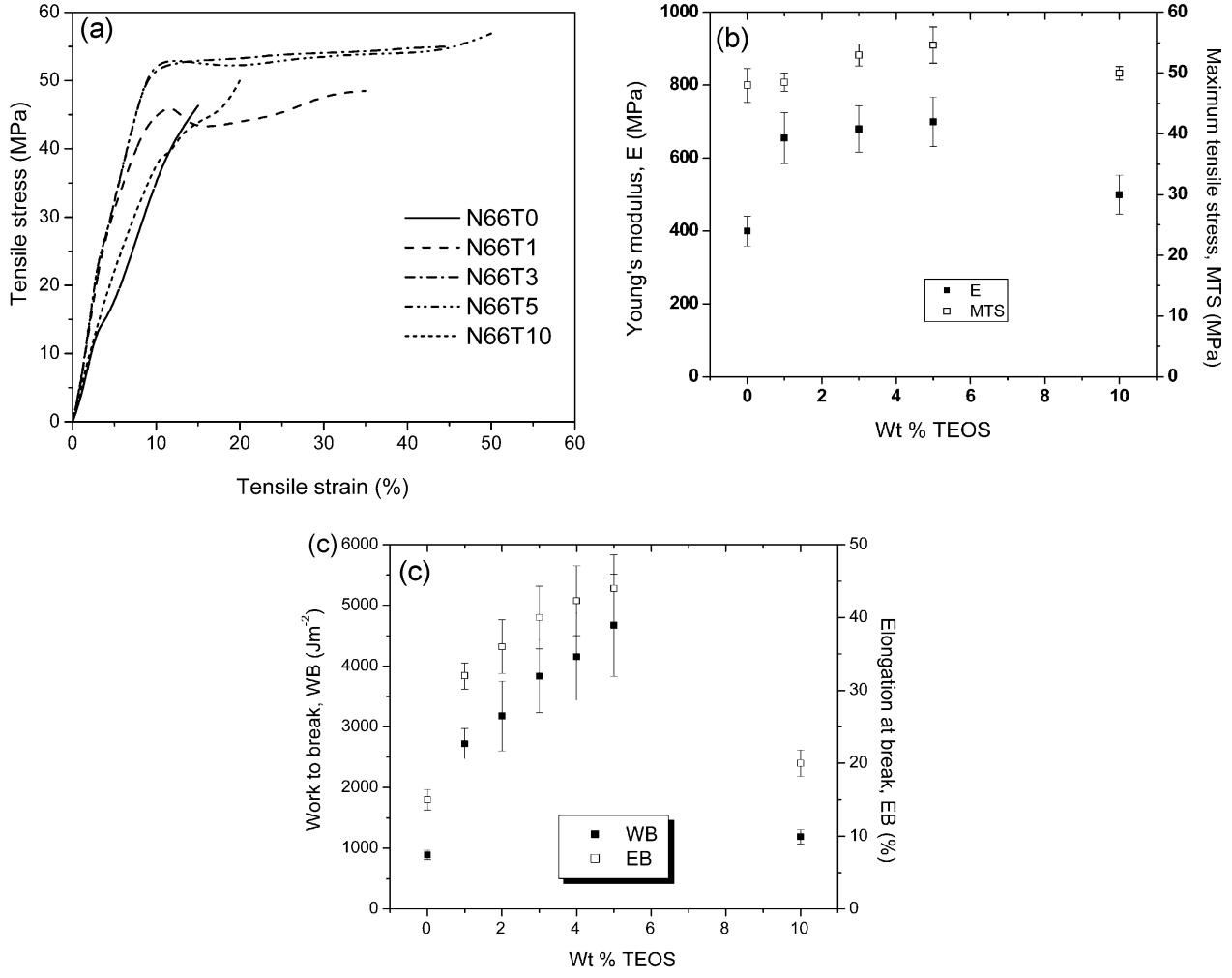


Fig. 8. (a) Representative tensile stress–strain curves for neat PA66 and PA66/silica nanocomposites. (b) Young's modulus and maximum tensile stress trends for neat PA66 and PA66/silica nanocomposites. (c) Work to break and elongation at break trends for neat PA66 and PA66/silica nanocomposites.

Fig. 9(b). The shift of the $T_g$ peak for the N66T5 film may be a result of optimization of the opposing effects of moisture absorption, decrease in free volume with increment in silica loading and reinforcement due to nanosized silica. The factors like free volume decrease with increment of silica loading, moisture-absorbing behavior and agglomeration of the silica probably determine the $T_g$ shift of N66T10. From Fig. 9(b) it is seen that the $E'$ values for the PA66/silica nanocomposites are above that of neat PA66 in the temperature range of −50–200 °C and can be explained on the basis of reinforcing action of nanosized in situ generated silica. Among all the composites, the N66T5 exhibits the highest storage modulus value. The lowering of the $E'$ trace for the N66T10 film compared to the N66T5 film can be explained on the basis of predominant effect of crystallinity decrease and silica agglomeration.

### 3.7. Water absorption behavior

The water uptake characteristics of unannealed neat PA66 and PA66/silica nanocomposites are compared in Fig. 10. It is well-known that PA66 is hydrophilic and tends to absorb water easily from the surrounding environment. From Fig. 10 it is seen that the nanocomposite films N66T1 and N66T3 have slightly higher water absorbing tendency than N66T0, whilst N66T5 and N66T10 have lower water absorbing tendency. This trend can be explained on the basis of two opposing factors: increased network structure formation on a volume basis as a result of increasing TEOS concentration leading to a decrease in free volume of the polymer and decrease in crystallinity with increasing TEOS loading. Initially the network structure formed is lower on a volume basis due to the lower quantity of TEOS loading and the crystallinity decrease as a result of TEOS loading (as evident from Table 3) also aids in increase in water absorption compared to N66T0. With increase in TEOS loading, the free volume of the polymer decreases as the polymerized silica fills up the free volume of the polymer. Therefore, the water uptake of the polymer decreases with the increment of silica loading.

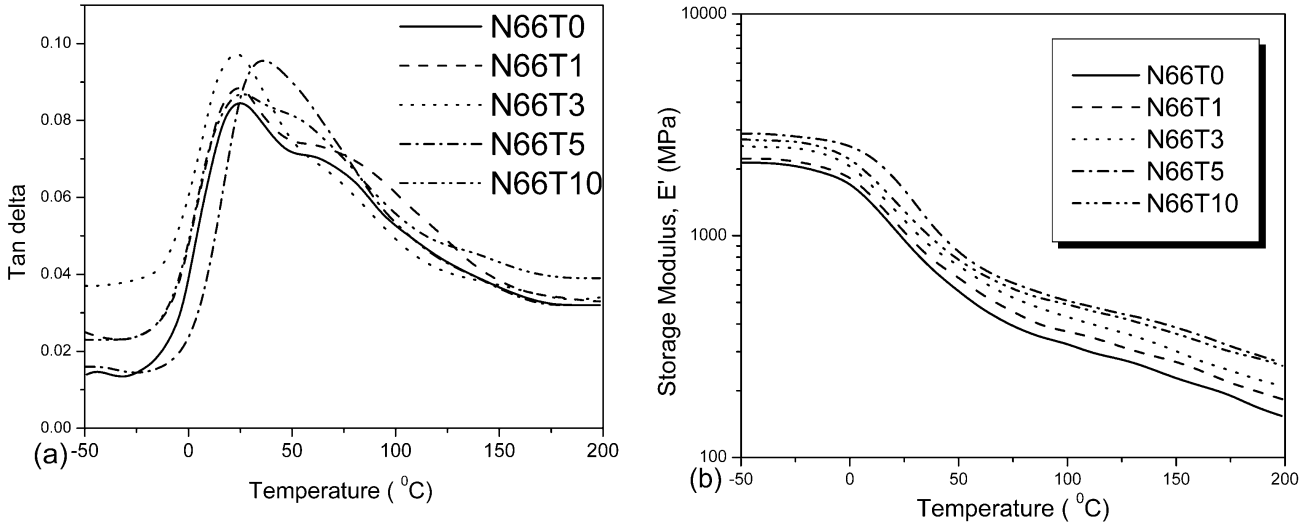


Fig. 9. (a) Tan $\delta$ curves for neat PA66 and PA66/silica nanocomposites. (b) Storage modulus ($E'$) curves of neat PA66 and PA66/silica nanocomposites.

## 4. Conclusions

PA66/silica hybrid nanocomposites were prepared by the sol–gel reaction between TEOS and PA66 matrix. IR studies revealed the formation of both linear and network silica growth structures. Dimensions of these silica structures were less than the optical wavelength and thus the hybrid films had optical clarity comparable to neat PA66 film. AFM studies further confirmed that one of the dimensions of the silica structures was within 100 nm and Si mapping revealed the homogeneity of the hybrid nanocomposites over the bulk of the matrix. WAXS of the films indicated the existence of the $\alpha$ and $\gamma$ phases. Crystallinity of the PA66/silica hybrid nanocomposites decreased with respect to neat PA66 with increasing TEOS loading. TGA results indicate that at very low loading of TEOS (less than 5% by weight of PA66) the thermal stability enhancement is substantial. However, negligible difference in the char residue of the films at 800 °C points at similar decomposition pathways for the hybrid and neat films. Improvement of mechanical property of the hybrid films is substantial compared to the neat film. However, optimization occurs at a TEOS loading of 5 wt% and this observation gets support from the DMA results. Brittleness of the hybrid films increases above TEOS loading of 10 wt%. Water absorption initially increases, but finally decreases with increment in TEOS loading due to the change in free volume of the polymer by the polymerized silica.

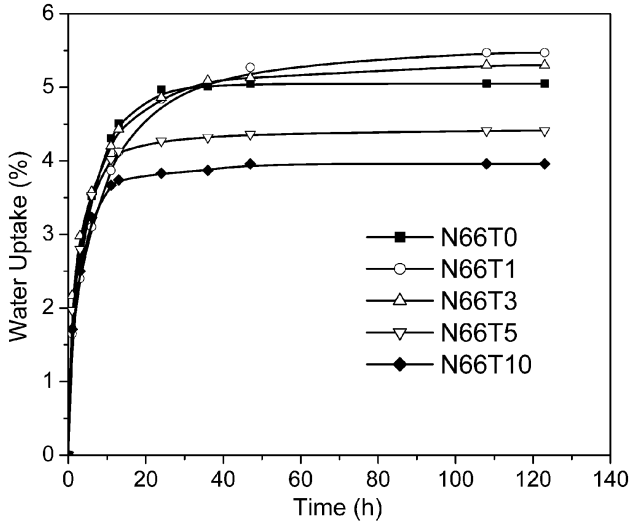


Fig. 10. Water uptake characteristics of neat PA66 and PA66/silica nanocomposites.

## Acknowledgements

We acknowledge the financial assistance provided by DAE, BRNS, Mumbai vide sanction no. 2002/35/7/BRNS/172. We are indebted to Mr Kausick Auddy and Mr Anirban Ganguly for the UV–Vis and AFM measurements. The AFM was acquired via an equipment grant from DST, New Delhi and MHRD, New Delhi, India.

## References

[1] Armelao L, Barreca D, Bottaro G, Gasparotto A, Tondello E, Ferroni M, Polizzi S. Chem Mater 2004;16:3331–8.
[2] Kim DS, Park HB, Rhim JW, Lee YM. J Membr Sci 2004;240:37–48.
[3] Schottner G. Chem Mater 2001;13:3422–35.
[4] Wen J, Wilkes GL. Chem Mater 1996;8:1667–81.
[5] Brinker CJ, Scherrer GW. Sol–gel science, the physics and chemistry of sol–gel processing. Academic Press: San Diego; 1990 [chapter 3].
[6] Fitzgerald JJ, Landry CJT, Pochan JM. Macromolecules 1992;25:3715–22.
[7] Landry CJT, Coltrain BK, Landry MR, Fitzgerald JJ, Long VK. Macromolecules 1993;26:3702–12.
[8] Landry CJT, Coltrain BK, Brady BK. Polymer 1992;33:1486–95.
[9] Landry CJT, Coltrain BK, Wesson JA, Zumbulyadis N, Lippert JL. Polymer 1992;33:1496–506.

[10] Ravaine D, Seminel A, Charbouillot Y, Vincens MJ. Non-Cryst Solids 1986;82:210–9.
[11] Sun CC, Mark JE. Polymer 1989;30:104–6.
[12] Mauritz KA, Warren RM. Macromolecules 1989;22:1730–4.
[13] Stefanithis ID, Mauritz KA. Macromolecules 1990;23:2397–402.
[14] Suzuki F, Onozato K, Kurokawa Y. J Appl Polym Sci 1990;39: 371–81.
[15] Sadhu S, Bhowmick AK. Rubber Chem Technol 2003;76:860–75.
[16] Sadhu S, Bhowmick AK. J Polym Sci, Polym Phys Ed 2004;42: 1573–85.
[17] Bandyopadhyay A, Bhowmick AK, De Sarkar M. J Appl Polym Sci 2004;93:2579–89.
[18] Bandyopadhyay A, De Sarkar M, Bhowmick AK. Rubber Chem Technol 2004;77:830–41.
[19] Okada A, Usuki A. Mater Sci Eng 1995;C3:109–15.
[20] Sengupta R, Tikku VK, Somani AK, Chaki TK, Bhowmick AK. Rad Phys Chem 2005;72:625–33.
[21] Turi EA, editor. Thermal characterization of polymeric materials. 2nd ed. San Diego: Academic Press; 1997.
[22] Murty EM, Yehl TW. Polym Eng Sci 1990;30:1595–8.
[23] Vasanthan N, Salem DR. J Polym Sci, Polym Phys Ed 2000;38: 516–24.
[24] Cooper SJ, Coogan M, Everall N, Priestnall I. Polymer 2001;42: 10119–32.
[25] Sanchez C, Ribot F. New J Chem 1994;18:1007–11.
[26] Bunn CW, Garner EV. Proc R Soc 1947;189A:39–51.
[27] Liu X, Wu Q, Berglund LA. Polymer 2002;43:4967–72.
[28] Hirschinger J, Miura H, Gardner KH, English AD. Macromolecules 1990;23:2153–69.
[29] Murthy NS, Curran SA, Aharoni SM, Minor H. Macromolecules 1991;24:3215–20.
[30] Jain A, Vijayan K. J Mater Sci 2002;37:2623–33.
[31] Haruvy Y, Rajbenbach LA, Jagur-Grodzinski J. Polymer 1984; 25(1431):1435.
[32] Khanna YP. Macromolecules 1992;25:3298–300.
[33] Wu TM, Liao CS. Macromol Chem Phys 2000;201:2820–5.
[34] Cho JW, Paul DR. Polymer 2001;42:1083–94.
[35] Zoppi RA, de Castro CR, Yoshida IVP, Nunes SP. Polymer 1997;38: 5705–12.